PROCEEDINGS OF SCIENCE

SuperTIGER Abundances of Galactic Cosmic Rays for the Atomic Number (Z) Interval 40 to 56

N.E. Walsh[*] **for the SuperTIGER collaboration**

Department of Physics and McDonnell Center for the Space Sciences, Washington University, St. Louis, MO 63130-4899, USA

E-mail: newalsh@wustl.edu

SuperTIGER (Super Trans-Iron Galactic Element Recorder) is a long-duration-balloon instrument that completed its first Antarctic flight during the 2012-2013 austral summer, spending 55 days at an average float altitude of 125,000 feet. SuperTIGER measured the relative abundances of Galactic cosmic-ray (GCR) nuclei with high statistical precision and well resolved individual element peaks from $_{10}$Ne to $_{40}$Zr. SuperTIGER also made exploratory measurements of the relative abundances up to $_{56}$Ba. GCR measurements up to $_{40}$Zr support a source acceleration model where supernovae in OB associations preferentially accelerate refractory elements that are more readily embedded in interstellar dust grains than volatiles. In addition, injection into the GCR for both refractory and volatile elements appears to follow a charge dependence consistent with their grain sputtering cross sections. Although statistics are low for elements heavier than $_{40}$Zr, our preliminary measurements of the $_{40}$Zr to $_{56}$Ba range suggest the existence of an alternative GCR source or acceleration model for these rare elements. We report progress in refining this interesting result.

38th International Cosmic Ray Conference (ICRC2023)
26 July - 3 August, 2023
Nagoya, Japan

[*]Speaker

PoS(ICRC2023)053

1. Introduction

Galactic cosmic-ray (GCR) elemental and isotopic abundance measurements are conducted to probe the composition of the Galactic cosmic-ray source (GCRS) and to place constraints on theories of the origin and acceleration of GCRs. The current model is that a majority of GCRs originate within OB associations, regions hosting numerous young, massive stars of spectral type O and B. This stellar environment leads to frequent supernovae (SNe) in close proximity [1], [2]. These SNe generate shock waves that collect and accelerate the surrounding interstellar medium (ISM) to GCR energies. The swept up ISM is enriched by massive star material (MSM) from stellar winds and prior SN explosions within the OB association.

Epstein 1980 [4] first described GCR acceleration in terms of volatility, where elements more inclined to embed in interstellar dust grains (refractory elements, with condensation temperatures $T_c > 1250$ K [5]) should experience a preferential acceleration compared to those elements that mainly exist in the form of interstellar gases (volatile elements, with $T_c < 1250$ K). In 2019, Lingenfelter further develops this explanation [3], by proposing that the observed atomic mass dependence seen in both volatile and refractory GCR element abundances arises from the atomic charge-dependent sputtering of these elements from the surfaces of the grains into which they condense. The underlying assumption of this theory is that *all* GCR particles are accelerated via dust grains, and the enhancement of refractory elements over volatiles stems from the higher probability of refractories to become embedded on grains. The mass-dependent enhancement observed in both GCR categories is subsequently explained by the likelihood of grain sputtering, driven by the charge-dependent ($\propto Z^{2/3}$) cross sections of the grain surface elements with charge Z interacting with ambient H and He, as in Figure 1.

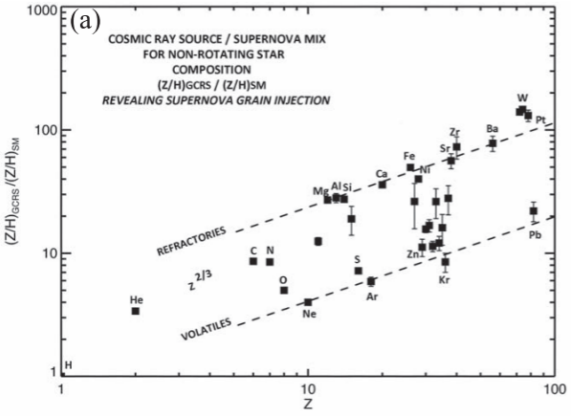

Figure 1: GCRS abundances for: Engelmann et al. 1990 & Cummings et al. 2016, $1 \leq Z \leq 28$; Rauch et al. 2009 & Murphy et al. 2016, $26 \leq Z \leq 40$; Binns et al. 1989, $40 \leq Z \leq 70$; Donnelly et al. 2012, $Z > 70$, plotted relative to a GCRS mixture of 20% MSM (Woosley and Heger 2007) and 80% SS (Lodders 2003). Normalized to an $_1$H ratio of 1. Figure from Lingenfelter 2019[3].

SuperTIGER made the first individual element resolution measurements of all GCR elements in the atomic charge range $30 \leq Z \leq 40$ [6]. As discussed here, and in Walsh et al. 2022 [7], our analysis has been extended to conduct the first GCR measurements of individual elements in the range $41 \leq Z \leq 56$. These observed abundances are reported as determined at the SuperTIGER instrument (Table 1). To obtain GCRS abundances, a series of corrections are necessary to account for changes in flux arising from nuclear interactions and energy losses occurring within the instrument, the atmosphere, and the ISM. These adjustments are required to obtain the elemental abundances of GCRs as they exist at the moment of acceleration from the GCRS. At present, our initial corrections allow discussion of preliminary science implications. In future work, we will improve these corrections in order to finalize the newest SuperTIGER GCRS abundances.

2. The SuperTIGER Instrument

The SuperTIGER instrument is optimized for measuring the relative abundances of ultra-heavy (UH) GCR nuclei and has performed single element measurements from $_{10}$Ne to $_{40}$Zr, exhibiting good statistics and individual-element charge resolution [6]. SuperTIGER employs a high and low gain readout for its Cherenkov detector photomultiplier tubes (PMTs) in addition to radically tapered voltage dividers for these and its scintillation detector PMT readouts. This design grants SuperTIGER a wide dynamic range, so it is capable of making single-element resolution abundance measurements up to $_{60}$Nd. During its 55-day Antarctic flight, SuperTIGER measured over 5 million cosmic-ray iron events, roughly 4500 events with $30 \leq Z \leq 40$, and 212 events with $41 \leq Z \leq 56$.

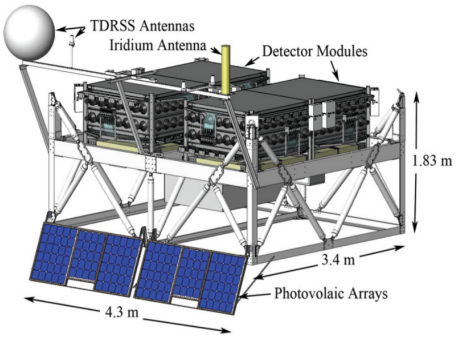

Figure 2: Technical model of the SuperTIGER payload with both instrument modules mounted in the gondola.

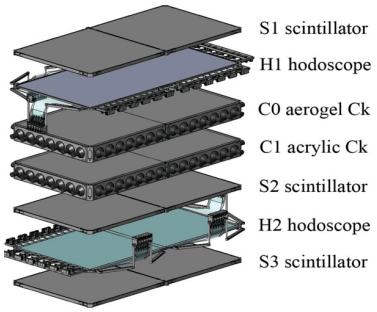

Figure 3: One module of the SuperTIGER instrument (expanded).

The SuperTIGER instrument [8] consists of two nearly identical modules (Figure 2), each housing seven stacked detectors, shown in Figure 3. Within each module, the stack includes, from top to bottom, a plastic scintillation detector (S1) responsible for charge determination and triggering coincidence, a scintillating optical fiber hodoscope plane (H1) capturing (x, y) position data near the top of the instrument, a silica-aerogel Cherenkov detector (C0), an acrylic Cherenkov detector (C1), both utilized for charge and energy determination, a second scintillation detector (S2) is used for charge determination and coincidence, followed by a second hodoscope plane (H2) detecting (x, y) position data near the bottom of the instrument. Lastly, a third scintillation detector (S3) primarily serves to reject particles that interact within the instrument, while also serving as a backup to S2 in case of its failure during flight. Combining signals from the S and C detectors allows for the measurement of the charge and kinetic energy of cosmic rays that traverse the entire stack without interaction. The position measurements from the two H layers are used to determine the trajectory of each cosmic ray through the instrument, which allows for angle corrections and detector area non-uniformity corrections.

3. Charge Assignment Method

SuperTIGER is designed to ensure excellent charge resolution for GCR events, spanning a wide energy range from approximately 320 MeV/nucleon to 10 GeV/nucleon. This is accomplished by employing two distinct charge assignment techniques that complement each other. These methods

each resolve charges for specific energy ranges: one is optimized for lower GCR energies below the aerogel threshold, and the other for higher GCR energies. The signals derived from each detector layer involved in charge determination for this analysis (S1, S2, C0, and C1) are obtained by summing the pedestal-subtracted, position and gain-corrected PMT signals in each layer. These signals, in turn, are adjusted for variations in angle and area responses. For each event, the detector signal then corresponds to the count of emitted photoelectrons by the charged particle as it passed through each detector. The Cherenkov light detector signals a charge dependence of nearly $C \propto Z^2$, while the scintillation light detector signal charge dependence is closer to $S \propto Z^{1.7}$.

When GCR events possess energies in the instrument greater than the Cherenkov threshold of the C0 detector (2.35 GeV/nucleon for three half modules and 3.31 GeV/nucleon for the fourth), we employ the "Above-C0" charge assignment method, which leverages signals from both the C0 and C1 detectors. In cases where the GCR energy falls below the C0 threshold yet remains above the C1 threshold (around 320 MeV/nucleon), the "Below-C0" charge assignment method is used. This method utilizes signals from two of the three scintillation detectors (S1 or S2) in conjunction with the C1 signal. For both the Above-C0 and Below-C0 methods, cross plots featuring these signals are generated, revealing well-resolved charge bands that can be subjected to analysis (Figures 4 and 5). In these plots, the highest visible band corresponds to nickel ($Z = 28$), while the dense band just beneath it is iron ($Z = 26$). Notice that the GCR elements heavier than nickel are too infrequent to form discernible charge bands. To measure the abundances of elements beyond nickel (including the exceedingly rare $41 \leq Z \leq 56$ range), we must accurately determine the charge dependence of the detector response using the visible charge bands and extrapolate this dependence into the UH range.

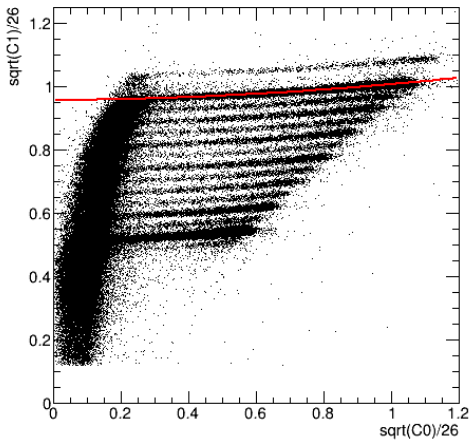

Figure 4: Quadratic fit to the Above-C0, C1 vs. C0 iron band for a half-module in module 2, with index of refraction $n = 1.043$.

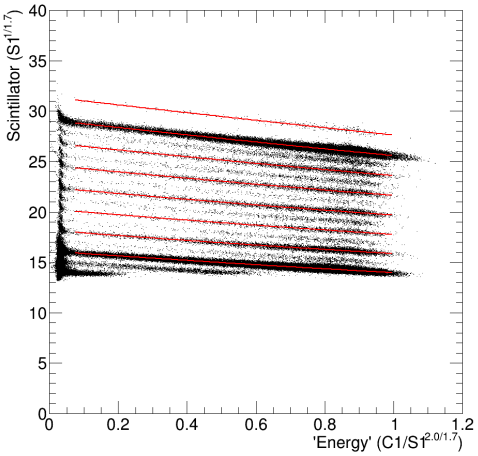

Figure 5: Quadratic fits to the Below-C0, S1 vs. $\xi = C1/S^{2/1.7}$ charge bands (even charges only).

3.1 Above-C0 Charge Assignment

For cosmic-ray events with energies surpassing the turn-on threshold of SuperTIGER's aerogel Cherenkov (C0) detector, the "Above-C0" method for charge assignment is employed. In the

C1 vs. C0 cross plots, as depicted in Figure 4, distinct charge bands emerge, characterized by seemingly equidistant, nearly straight lines. It can be demonstrated that, given a sample of GCR events each producing two pure Cherenkov signals in distinct radiating materials, these events should align along a series of parallel lines (or bands) separated based on charge ($\propto Z^2$). In essence, a single equation describing a solitary charge band suffices to establish the equations governing all other charge bands formed from signals derived from the same pair of Cherenkov detectors. To characterize this phenomenon, we examine the band corresponding to iron nuclei, as its vicinity to the UH region allows for the best extrapolation to the very high charges. It's important to acknowledge that the charge bands, although predominantly linear, exhibit slight deviations attributed to minor contributions from scintillation in detector materials, Cherenkov emission from delta rays, in addition to Cherenkov emission from the cosmic ray itself. These deviations are effectively captured by the quadratic fit employed. Armed with the functional representation of the bands and the associated C0 and C1 values within this signal space, we are able to compute the charge of all incident particles in the "Above-C0" data set.

3.2 Below-C0 Charge Assignment

For cosmic-ray events characterized by energies falling below the operational threshold of SuperTIGER's aerogel Cherenkov (C0) detectors, the "Below-C0" method for charge assignment is implemented. The light emitted by a scintillating material represents a fraction of the energy (dE/dx) deposited by a charged particle while traversing the radiating material. This dE/dx adheres to the Bethe-Bloch equation and showcases a straightforward reliance on the charge of the moving particle (Z^2). However, the kinetic energy dependence of the energy deposition is notably more intricate. Additionally, the saturation of emission sites within the scintillator, occurring when substantial energy deposits are concentrated within a small region, reduces the anticipated light yield (dL/dx) and introduces deviations in the charge dependence of the measured signal from the Bethe-Bloch equation. This saturation effect is itself contingent on charge, necessitating the modeling of $dL/dx(Z)$ to accurately deduce event charges. In essence, in the "Below-C0" method, a sole charge band fit no longer suffices to encapsulate the shape and spacing of the remaining bands, as seen in the "Above-C0" method, where the Z^2-dependent separation of bands is reliable. To effectively model the Below-C0 $dL/dx(Z)$, which includes energy dependency and saturation influences, a manual determination of band separation is required, so fitting across a series of charge bands is performed.

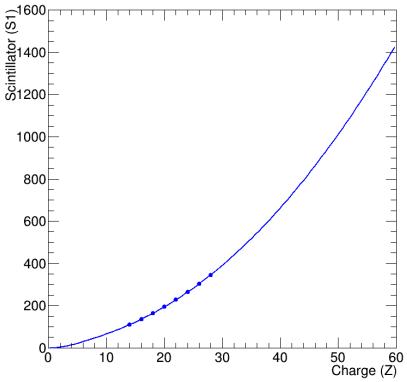

Figure 6: The simplified Tarle saturation model (Equation 1) fit to S1 vs. Z points for a sample angle-ξ bin combination.

$$S = AZ^2 + \frac{BZ^2}{1 + CZ^2} \qquad (1)$$

Within each angle bin, we plot scintillator signals against an energy proxy, denoted as $\xi = C1/Z^2 \approx C1/S^{2/1.7}$, and segment the charge bands into ξ bins. Each ξ bin is constructed to hold and equal number of iron events. For every angle bin, a quadratic fit is employed to approximate the shape of each even-charge band in the S vs. ξ domain. Then, within each ξ bin, we apply

a simplified ($d\beta/dx = 0$) saturation model to the S vs. Z data points (as illustrated in Figure 6), determined by the spacing of even-charge bands within each angle-ξ bin. This simplified Tarle model takes the form in Equation 1, where S is the scintillator signal, Z is the charge of the incident particle, and A, B, and C are fit parameters. The parameters derived from the simplified Tarle model fits are preserved for every combination of angle and ξ bin. These parameters serve as the basis for constructing a charge surface over angle-ξ space via bilinear interpolation. This resultant charge surface is then used to assign charges to particles characterized by their S and C1 signals in any angle-ξ combination.

3.3 Measured Instrument Abundances

To determine elemental abundances at the instrument level, the combined charge histogram generated from the Above- and Below-C0 methods undergoes a maximum likelihood fitting process using a multi-peak Gaussian function. This composite function incorporates 41 Gaussian peaks, each corresponding to a specific charge within the range of $16 \leq Z \leq 56$. During the fitting procedure, the position of the first peak (at $Z = 16$) and the peak separation are adjustable, while the sigma of the Gaussian peaks is assumed to vary linearly with Z. The outcome of the fit yields a first peak position at $Z = 16.0070$ and a peak separation of 1.00005 charge units (c.u.). The sigma values established for the peaks at $Z = 16$, $Z = 26$, and $Z = 56$ are 0.179, 0.185, and 0.203 c.u., respectively. The resulting fit for the newly measured range is presented in Figure 7. Finally, the elemental abundances, as measured within the SuperTIGER instrument, are calculated from the areas under each Gaussian peak. As a consistency check, the abundances computed by the fit for $40 \leq Z \leq 56$ are cross-referenced with the histogram counts integrated for each element within this range. For each value of Z, the histogram counts are summed within the interval $Z \pm 0.5$ c.u. This comparison is detailed in Table 1. The abundances derived through the fit closely align with the integrated histogram counts for each element, as the sum of all $40 \leq Z \leq 56$ abundances only slightly exceeds the integrated histogram count by 1.1 particles.

Z	N_{INST}	N_{HIST}
40	53.6	53
41	17.0	17
42	29.2	28
43	14.1	15
44	22.4	22
45	6.6	7
46	13.7	13
47	5.7	6
48	6.5	7
49	6.0	6
50	24.9	25
51	5.1	5
52	18.1	17
53	4.9	6
54	9.9	9
55	5.2	6
56	11.1	11
SUM	254.1	253

Table 1: Fit-determined instrument abundances for $40 \leq Z \leq 56$ compared to histogram counts within $Z \pm 0.5$ c.u. for each integer charge.

4. Preliminary Science Implications

The obtained abundances are adjusted for interactions and energy losses that occur within the instrument, atmosphere, and ISM, yielding the abundances as they exist at the top of the instrument (TOI), at the top of the atmosphere (TOA), and at the GCRS. Currently, these corrections remain in a preliminary state and necessitate further refinement to finalize the SuperTIGER GCRS abundances for the $40 \leq Z \leq 56$ range. These revisited corrections will be completed as future work, but, for now, we discuss possible science implications of the preliminary SuperTIGER GCRS abundances.

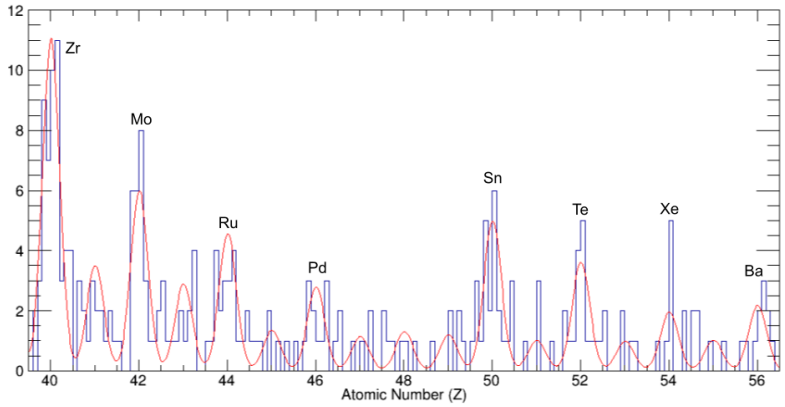

Figure 7: SuperTIGER's newly measured charge range, $41 \leq Z \leq 56$, with multi-peak Gaussian fit result. A linear scale is used for this low statistics region.

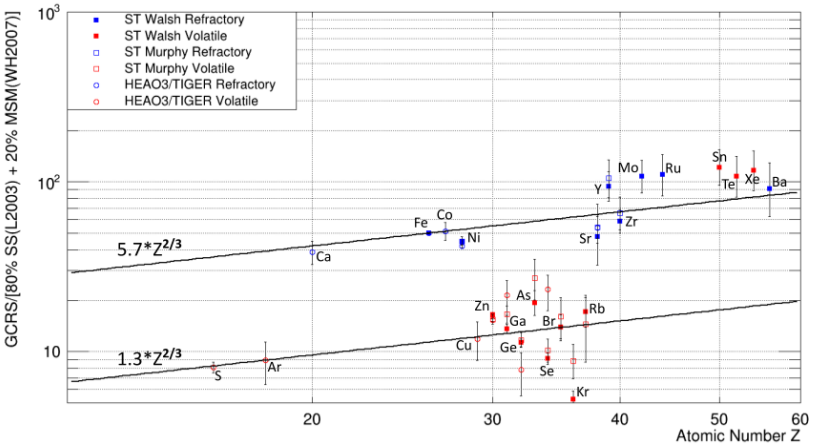

Figure 8: SuperTIGER GCRS abundances plotted relative to an OB association representative mix of 80% solar system material (Lodders 2003[9]) and 20% massive star material (Woosley and Heger 2007[10]). Odd elements with $Z > 40$ are removed along with $Z = 46$ and 48 due to poor statistics and large systematic uncertainties.

To evaluate the validity of the OB association GCR origin and acceleration model, we compare the GCRS abundances with a representative composition of 80% solar system material and 20% massive star material (as shown in Figure 8). As expected, elements up to ${}_{40}$Zr exhibit distinct differentiation between refractory and volatile components. However, the refractory preferential acceleration model does not seem to hold true for elements heavier than ${}_{40}$Zr. Specifically, it appears that, while the volatile elements within $40 \leq Z \leq 56$ still follow a $\propto Z^{2/3}$ charge-dependence, they appear to be boosted up to the refractory enhancement line.

The apparent breakdown of the refractory preferential acceleration model for elements in the $40 \leq Z \leq 56$ range raises the possibility of an alternative production site or acceleration mechanism for these elements. Additional investigation is necessary to explore this observed deviation in the GCRS model.

References

[1] H. Reeves. Nucleosynthesis and the Origin of the Galactic Cosmic Rays. *Proceedings of the 13th International Cosmic Ray Conference*, 5:3323–3353, 1973.

[2] J. C. Higdon and R. E. Lingenfelter. OB Associations, Supernova-Generated Superbubbles, and the Source of Cosmic Rays. *The Astrophysical Journal*, 628:738–749, 2005.

[3] Richard E. Lingenfelter. The Origin of Cosmic Rays: How Their Composition Defines Their Source and Sites and the Process of Their Mixing, Injection, and Acceleration. *The Astrophysical Journal Supplement Series*, 245:30, 2019.

[4] Richard I. Epstein. The Acceleration of Interstellar Grains and the Composition of the Cosmic Rays. *Monthly Notices of the Royal Astronomical Society*, 193(4):723–729, 1980.

[5] Donald C. Ellison, Luke O'C. Drury, and Jean-Paul Meyer. Galactic Cosmic Rays from Supernova Remnants. II. Shock Acceleration of Gas and Dust. *The Astrophysical Journal*, 487:197–217, 1997.

[6] R. P. Murphy, M. Sasaki, W. R. Binns, T. J. Brandt, T. Hams, M. H. Israel, A. W. Labrador, J. T. Link, R. A. Mewaldt, J. W. Mitchell, B. F. Rauch, K. Sakai, E. C. Stone, C. J. Waddington, N. E. Walsh, J. E. Ward, and M. E. Wiedenbeck. Galactic Cosmic Rays Origins and OB Associations: Evidence from SuperTIGER Observations of Elements $_{26}$Fe through $_{40}$Zr. *The Astrophysical Journal*, 831(2):148, 2016.

[7] N. E. Walsh, Y. Akaike, W. R. Binns, R. G. Bose, T. J. Brandt, D. L. Braun, N. W. Cannady, P. F. Dowkontt, T. Hams, M. H. Israel, J. F. Krizmanic, A. W. Labrador, R. A. Mewaldt, J. W. Mitchell, R. P. Murphy, G. A. de Nolfo, S. Nutter, M. A. Olevitch, B. F. Rauch, K. Sakai, M. Sasaki, G. E. Simburger, E. C. Stone, T. Tatoli, J. E. Ward, M. E. Wiedenbeck, and W. V. Zober. SuperTIGER instrument abundances of galactic cosmic rays for the charge interval $41 \leq Z \leq 56$. *Advances in Space Research*, 70(9):2666–2673, 2022.

[8] W. R. Binns, R. G. Bose, D. L. Braun, T. J. Brandt, W. M. Daniels, P. F. Dowkontt, S. P. Fitzsimmons, D. J. Hahne, T. Hams, M. H. Israel, J. Klemic, A. W. Labrador, J. T. Link, R. A. Mewaldt, J. W. Mitchell, P. Moore, R. P. Murphy, M. A. Olevitch, B. F. Rauch, K. Sakai, F. San Sebastian, M. Sasaki, G. E. Simburger, E. C. Stone, C. J. Waddington, J. E. Ward, and M. E. Wiedenbeck. The SuperTIGER Instrument: Measurement of Elemental Abundances of Ultra-Heavy Galactic Cosmic Rays. *The Astrophysical Journal*, 788:18, 2014.

[9] Katharina Lodders. Solar System Abundances and Condensation Temperatures of the Elements. *The Astrophysical Journal*, 519:1220–1247, 2003.

[10] S. E. Woosley and A. Heger. Nucleosynthesis and Remnants in Massive Stars of Solar Metallicity. *Physics Reports*, 442:269–283, 2007.

Full Authors List: SuperTIGER Collaboration

Y. Akaike[1], W. R. Binns[2], R. G. Bose[2], T. J. Brandt[3], D. Braun[2], N. Cannady[4,5,6], P. F. Dowkontt[2], T. Hams[4,5,6], M. H. Israel[2], J. F. Krizmanic[4,5,6], A. W. Labrador[7], R. A. Mewaldt[7], J. W. Mitchell[5] R. P. Murphy[2], G. A. de Nolfo[8], N. E. Osborn[2] B. F. Rauch[2], K. Sakai[4,5,6], M. Sasaki[5,6,9], G. Simburger[2], E. C. Stone[7], T. Tatoli[8,10], N. E. Walsh[2], J. E. Ward[2], M. E. Wiedenbeck[11,7], W. V. Zober[2],

[1]Waseda Research Institute for Science and Engineering, Waseda University, Tokyo 162-0044, Japan

[2]Department of Physics and McDonnell Center for the Space Sciences, Washington University, St. Louis, MO 63130-4899, USA

[3]NASA Goddard Space Flight Center, Greenbelt, MD 20771, USA

[4]Center for Space Sciences and Technology, University of Maryland Baltimore County, Baltimore, MD 21250, USA

[5]Astroparticle Physics Laboratory, NASA/GSFC, Greenbelt, Maryland 20771, USA,

[6]Center for Research and Exploration in Space Sciences and Technology, NASA/GSFC, Greenbelt, MD 20771, USA

[7]California Institute of Technology, Pasadena, CA 91125, USA

[8]Heliospheric Physics Laboratory, NASA/GSFC, Greenbelt, Maryland 20771, USA,

[9]Department of Astronomy, University of Maryland, College Park, Maryland 20742, USA,

[10]Department of Physics, Catholic University of America, Washington, DC 20064, USA

[11]Jet Propulsion Laboratory, Pasadena, CA 91109, USA

PoS(ICRC2023)053